International Journal of Nanomedicine

Dovepress
Taylor & Francis Group

Open Access Full Text Article

ORIGINAL RESEARCH

Engineering Study on Targeted Therapy of Osteosarcoma Using Tripterine Loaded Polydopamine Mesoporous Microspheres Combined with Photothermal Therapy

Molin Li[1,2,*], Yufei Ma[3,*], Hui Yao[1], Hao Jia[1], Yalan Wang[2,*], Xuefeng Tang[1,*]

[1]Department of Pathology, Chongqing General Hospital, Chongqing University, Chongqing, 401147, People's Republic of China; [2]Department of Pathology, College of Basic Medicine, Chongqing Medical University, Chongqing, 400016, People's Republic of China; [3]Research Center of Stem Cells and Ageing, Chongqing Institute of Green and Intelligent Technology, Chinese Academy of Sciences, Chongqing, 400714, People's Republic of China

*These authors contributed equally to this work

Correspondence: Yalan Wang, Department of Pathology, College of Basic Medicine, Chongqing Medical University, Chongqing, 400016, People's Republic of China, Email wangyalan0505@163.com; Xuefeng Tang, Department of Pathology, Chongqing General Hospital, Chongqing University, Chongqing, 401147, People's Republic of China, Email txfaaty@163.com

Purpose: Osteosarcoma poses significant clinical challenges due to its high recurrence, metastatic potential, and poor prognosis. Celastrol (CLT), known for its antitumor, immunomodulatory, and osteogenic regulatory properties, has garnered substantial interest. Developing a targeted CLT delivery system is critical to enable precise drug release, integrate photothermal therapy, remodel the tumor microenvironment, and improve post-surgical treatment and repair in osteosarcoma.

Methods: Using emulsion-induced interface assembly, we synthesized mesoporous polydopamine-polyethylene glycol (MPDA-PEG) nanospheres and loaded them with celastrol to fabricate the targeted system MPDA-PEG-CLT. We characterized the nanospheres' physicochemical properties and evaluated MPDA-PEG-CLT's efficacy in synergistic drug-photothermal therapy for osteosarcoma through in vitro and in vivo experiments.

Results: MPDA-PEG-CLT achieved a drug loading capacity of ~14% and a photothermal conversion efficiency of 37.6% under 808 nm NIR irradiation, which enhanced celastrol release. The system induced osteosarcoma cell apoptosis, promoted bone marrow mesenchymal stem cell (BMSC) differentiation, and ameliorated the lesion microenvironment, resulting in efficient tumor ablation in mice.

Conclusion: MPDA-PEG-CLT significantly enhances celastrol's targeted delivery efficiency, promotes mitochondrial apoptosis in osteosarcoma cells, synergizes with photothermal therapy to eradicate tumors, and improves the bone tissue microenvironment in lesions. This system offers a promising strategy for post-surgical osteosarcoma treatment and repair.

Keywords: photothermal therapy, mesoporous polydopamine, celastrol, mitochondrial apoptosis

Introduction

Osteosarcoma is a common primary malignant bone tumor characterized by high malignancy, strong metastatic propensity, and poor prognosis, posing persistent challenges to clinical treatment.[1] Surgical intervention remains the primary treatment modality for osteosarcoma, yet outcomes remain suboptimal, with a 5-year survival rate below 20%. Adjuvant chemotherapy agents such as methotrexate (MTX), doxorubicin (ADR), and cisplatin (DDP) are employed to mitigate metastasis and recurrence post-surgery. However, the unique bone tissue microenvironment enhances tumor cell resistance to radiotherapy and chemotherapy, significantly compromising therapeutic efficacy.[2] Hypoxia, acidic conditions, and cancer-associated fibroblasts (CAFs) in the tumor microenvironment remodel the extracellular matrix (ECM), increasing tissue density and creating physical barriers that impede drug penetration.[3] In addition, the interaction of osteoblasts and osteoclasts in the tumor microenvironment may also

Received: 4 April 2025
Accepted: 12 September 2025
Published: 24 September 2025

Graphical Abstract

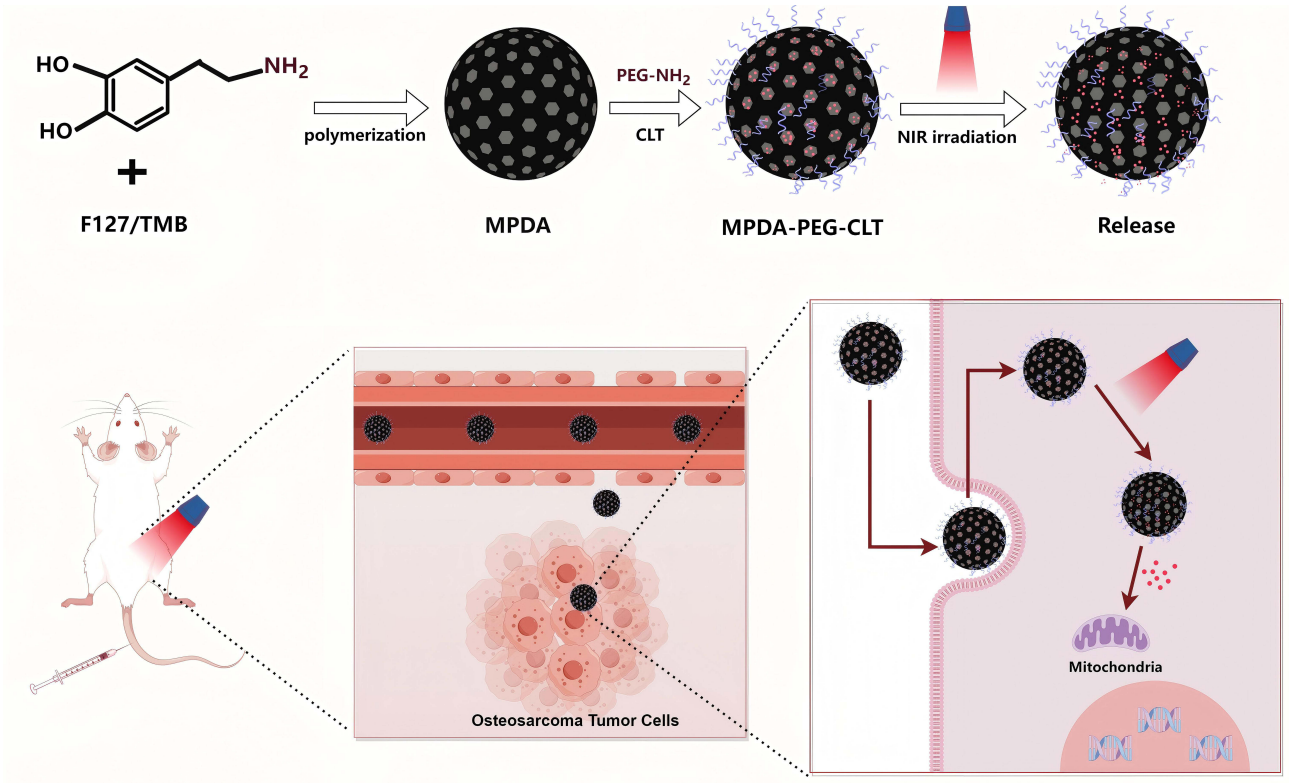

play a role in resistance mechanisms.[4] It has led to drug resistance in osteosarcoma cells and triggered adverse side effects. Consequently, there is an urgent need to explore novel therapeutic strategies to improve osteosarcoma treatment outcomes.

Celastrol (CLT), a natural bioactive compound, has been demonstrated to play critical roles in immune and neurodegenerative diseases.[5] Recent research indicates that CLT can induce apoptosis in tumor cells and influence osteosarcoma cell fate via pathways such as mevalonate and endoplasmic reticulum stress,[6,7] positioning it as a promising candidate for osteosarcoma chemotherapy. Remarkably, CLT also regulates the bone tissue microenvironment by enhancing PGC-1α signaling, thereby promoting osteogenic differentiation of bone marrow mesenchymal stem cells (BMSCs).[8] These exceptional biological properties suggest CLT's potential for eradicating residual tumor cells and reconstructing lesion areas post-surgery. However, systemic administration of CLT is limited by severe organ toxicity, poor aqueous solubility, and low intestinal permeability, which diminishes the efficacy of oral administration and restricts its clinical applicability.[9] Thus, developing strategies for precise targeted delivery of CLT that maximize therapeutic efficacy while minimizing side effects is a focal point of current research.

Nanoparticle delivery systems offer advantages such as targeted delivery, sustained release, and synergistic effects, effectively enhancing the antitumor activity of loaded drugs.[10,11] Metal-organic frameworks (MOFs) exemplify this approach by addressing drug insolubility and enabling tumor microenvironment-responsive release, while macrophage-derived cellular vesicles (MCVs) leverage inherent tumor-homing capabilities for precision delivery.[3,12] Among these, polydopamine (PDA) nanospheres are noted for their simplicity in synthesis, ease of modification, and broad application across chemistry, biology, medicine, and materials science.[13–15] They can encapsulate various active agents such as chemotherapeutic drugs, photosensitizers, genes, and immunosuppressants via physical adsorption or chemical conjugation, facilitating applications in chemotherapy, photodynamic therapy, and immunotherapy.[16] Moreover, PDA microspheres exhibit excellent near-infrared (NIR)-induced photothermal effects. When integrated with targeted drug delivery,

they hold promise as a synergistic approach for osteosarcoma treatment, overcoming the limitations of traditional chemotherapy.[17,18] Elevated temperatures at the tumor site can further enhance drug release and increase the sensitivity of tumor cells to the therapeutic agents.

PDA's ability to bind aromatic drugs through non-covalent π-π and hydrogen bond interactions makes it an ideal carrier for CLT, forming innovative nano-targeted drug delivery systems,[19] The mesoporous structure of PDA nanospheres significantly improves the drug loading capacity (DLC), facilitating efficient loading of CLT. This design aligns with advanced nanocarrier strategies that leverage material properties (eg, MOF porosity, PDA π-π stacking) to optimize drug loading and controlled release.[12]

In this study, we synthesized folic acid-modified polydopamine (MPDA-PEG) nanospheres with mesoporous structure and utilized it for CLT loading to develop a drug-photothermal combination therapy for postoperative osteosarcoma treatment. We characterized the photothermal efficiency, drug loading, and release kinetics of this nano-delivery system. The therapeutic efficacy and mechanisms of MPDA-PEG-CLT were investigated using in vitro cell cultures and in vivo mouse models. Importantly, MPDA-PEG-CLT facilitates targeted delivery of CLT, thereby mitigating organ toxicity and overcoming osteosarcoma resistance to traditional chemotherapeutics.

Materials and Methods

Material

Dopamine hydrochloride, Pluronic F127, 1,3,5-trimethylbenzene were purchased from Aladdin Biotechnology Co., Ltd. (Shanghai, China). Celastrol (CLT), NH_2 · PEG · FA (97% average Mw 2000) were purchased from Shanghai McLaren Biochemical Technology Co., Ltd. Acetone, hydrogen peroxide (30%, H_2O_2), absolute ethanol and ammonia (25% ~ 28%, NH_3 · H_2O) were purchased from China Medicinal Chemical Reagent Co., Ltd. (Shanghai, China). Osteosarcoma cell line 143B was purchased from the Cell Bank of Type Culture Collection Committee of Chinese Academy of Sciences (Catalog No.: TCHu264). Dimethyl sulfoxide (DMSO) was purchased from Sigma-Aldrich (St. Louis, USA).4,6-diamidino-2-phenylindole (DAPI), calcein acetylmethoxy (AM) and propidium iodide (PI), and mitochondrial membrane potential and apoptosis detection kits (Mito-Tracker Red CMXRos and Annexin V-FITC) were purchased from Biyuntian Biotechnology Co., Ltd. (Shanghai, China). CCK-8 reagent was purchased from DojinDo, Japan. Cyanamide dye (CY5-amine) was purchased from Chongqing Yuqi Medical Technology Co., Ltd. (Chongqing, China). Rabbit polyclonal antibody to Cleaved-Caspase 3, Rabbit polyclonal antibody to Cleaved-Caspase 9, Rabbit polyclonal antibody to Bax, Rabbit polyclonal antibody to Bcl-2 were purchased from Affinity Biotechnology Co., Ltd. (Jiangsu, China). Goat Anti-Rabbit IgG HampL antibody was purchased from Beijing Boosen Biotechnology Co., Ltd. (Beijing, China).

Cytochrome C Mouse Monoclonal Antibody (Cytochrome C), Tomo20, and Alexa Fluor ® 488 Conjugate, Alexa Fluor ® 594 Conjugate antibodies were purchased from Cell Signaling Technology (Danvers, USA). All chemicals were used as received without further purification.

Synthesis and Surface Modification of Mesoporous Polydopamine Nanospheres (MPDA)

MPDA nanospheres were synthesized using a modified emulsion induced interface assembly method,[20] 1.2 g F127, 1 g dopamine hydrochloride, and 1.6 mL TMB were added and sonicated to form an emulsion in a mixture of 50 mL water and 50 mL ethanol. Then, 2 mL of ammonia was added and stirred at 60 ° C for 3 h. The reaction products were collected by centrifugation and washed several times with water to obtain MPDA particles with a particle size of approximately 80 nm. Different sizes of MPDA can be achieved by changing the reaction temperature (20 ° C, ~ 200 nm). In order to improve the surface properties of MPDA and enable it to target osteosarcoma cells, MPDA was modified using NH2-PEG-FA (97% mean Mw 2000) and filtered through a dialysis bag with a molecular weight cut-off of 10,000 Da to remove excess NH2-PEG-FA, and the resulting MPDA-PEG nanospheres were placed at 4 ° C for subsequent experimental use.

Characterization

Transmission electron microscopy (TEM) images of nanospheres as well as elemental analysis were taken on a transmission electron microscope (JEOL JEM-F200, Japan) by dropping the solution onto a carbon-coated copper mesh at an acceleration of 10 KV. Nanoparticle size as well as zeta potential were measured using a Malvern Zetasizer Nano ZS90 analyzer (Malvern Instruments, UK). Specific surface area as well as pore size distribution and pore volume of the samples were measured using a fully automated specific surface and porosity analyzer (Micromeritics ASAP 2460, USA). Fourier Transform Infrared Spectroscopy (FT-IR) was measured using a Fourier Transform Infrared Spectrometer (Thermo Fisher Scientific Nicolet iS20, USA). Raman spectroscopy was measured using a laser Raman spectrometer (Thermo Scientific DXR, USA) with an excitation wavelength of 532 nm. The photothermal effect test was performed using an 808 nm continuous near-infrared laser (Shenzhen Infrared Laser Technology Co., Ltd., China) with a spot size of 8 mm and 10 mm. Thermal imaging pictures were taken using a high-precision infrared thermal imager (guide-sensmart, China).

Biodegradability Test

Hydrogen peroxide solution (5 mM 10 mM) was mixed with MPDA suspension (100 μg/mL) and stirred for 24 hours, and samples were taken every 1 hour. Biodegradability was then evaluated using absorbance at 808 nm.

Photothermal Performance Determination

100 μL of MPDA-PEG (100 μg/mL) nanospheres were instilled into a 96-well plate. Temperature was measured with an infrared imager after irradiation with a 808 nm continuous near-infrared laser (2 W cm^{-2}) for 5 min. The photothermal conversion efficiency (η) of MPDA-PEG nanospheres was determined according to a reported method.[21] Detailed calculations are as follows:

$$\eta = \frac{\mathrm{hS}\Delta\ \mathrm{Tmax} - \mathrm{Qs}}{\mathrm{I}\left(1 - 10^{-\mathrm{A}}\right)} = \frac{\mathrm{hS}(\Delta\ \mathrm{Tmax} - \Delta\ \mathrm{Tmaxs})}{\mathrm{I}\left(1 - 10^{-\mathrm{A}}\right)}$$

$$\mathrm{hS} = \frac{msCs}{\tau}$$

In the above formula, h is the heat transfer coefficient, S is the surface area of the vessel, and ΔTmax is the temperature change of the nanoparticle suspension at the highest steady-state temperature. ΔTmaxs indicates the temperature change of the solvent (eg, H_2O) at the maximum steady-state temperature; Qs indicates the heat associated with the near-infrared light absorbance of the solvent. I is the incident laser density (2w cm^{-2}) and A is the absorbance of the nanospheres at 808 nm. τ is the sample system time constant and can be determined by linear curve fitting of the temperature cooling time to its ln ΔT/ΔTmax. ms and Cs are mass and heat capacity of the solvent (pure water), respectively.

CLT Load and Release Determination

In order to load CLT into the mesoporous channel of MPDA-PEG, 10 mg of MPDA-PEG nanospheres with 3 mg of CLT were dispersed into 3 mL of acetone and stirred at room temperature, and after evaporation of two-thirds volume of acetone, CLT-loaded MPDA-PEG nanospheres (MPDA-PEG-CLT) were collected by centrifugation and washed three times with deionized water to remove surface-adsorbed CLT. To determine the drug loading capacity (DLC) versus encapsulation efficiency of MPDA-PEG-CLT, 100 μL of MPDA-PEG-CLT was eluted with 400 μL of distilled water and the eluate was passed through a Sephadex G50 column three times. The UV absorption value (m2) of CLT in MPDA-PEG was also measured at 425 nm using a UV-Vis spectrophotometer. Then, 100 μL of MPDA-PEG-CLT was diluted with 400 μL of distilled water to directly determine the UV absorption value (m1) of total CLT, and the total amount of MPDA-PEG-CLT was m3. The encapsulation efficiency and drug loading rate were calculated according to the following formula:

$$\text{Encapsulation efficiency} = \frac{\text{m1} - m2}{\text{m1}} \times 100\%$$

$$\text{Drug loading rate} = \frac{\text{m1} - m2}{\text{m3}} \times 100\%$$

To investigate the release properties of CLT, 5 mg MPDA-PEG-CLT nanospheres were dispersed in 5 mL PBS. Samples were then transferred to dialysis bags which were dialyzed against 20 mL PBS buffer and shaken in a dark environment. Every hour, 2 mL of the solution was withdrawn from the solution and supplemented with 2 mL of fresh PBS. All drug release results were averaged over triplicate measurements. To investigate the effect of NIR irradiation on drug release performance, MPDA-PEG-CLT (1 mg mL^{-1}) was incubated under NIR irradiation, and the release concentration of CLT was measured at 425 nm using a UV-Vis spectrophotometer.

In vitro Cell Viability Assay

143B cells (human osteosarcoma cell line) were cultured in DMEM medium containing 10% (v/v) fetal bovine serum. MSCs (mouse bone marrow stromal cells) were cultured in MEM medium containing 10% (v/v) fetal bovine serum. Cells were incubated in 96-well culture plates for 24 hours. Subsequently, cells were treated with different concentrations of MPDA-PEG nanoparticle dispersions and incubated for 24 hours. Finally, cell viability was determined using CCK-8 assay.

Cellular Uptake Assay

Cy5-modified MPDA-PEG nanospheres were prepared in cell uptake experiments by mixing 20 mg MPDA-PEG nanospheres with 5 mg CY5-amine in a dimethylsulfoxide (DMSO)/PBS (v/v, 1/99) solution and magnetically agitated in the dark for 24 hours. The cellular uptake capacity of Cy5-modified MPDA-PEG-CLT nanospheres was determined by inverted fluorescence microscopy. 143B cells were cultured with MSCs cells in 24-well plates for 12 h and co-incubated with Cy5-modified MPDA-PEG nanospheres for 4 h. Cells were then stained with DAPI for 15 min before fluorescent images were taken using an inverted fluorescence microscope.

Vitro PTT And Chemotherapeutic Assay

143B cells were seeded in 96-well plates and incubated for 24 h before group treatment. For the MPDA-PEG + Laser and MPDA-PEG- CLT + Laser groups, 143B cells were treated with MPDA-PEG/MPDA-PEG-CLT nanospheres for 4 h and irradiated with a near-infrared laser (808 nm, 2Wcm^{-2}) for 5 min. The treatment effect was then measured after an additional 24 hours of incubation. In order to determine the therapeutic effect of MPDA-PEG, CLT, and MPDA-PEG-CLT groups, MPDA-PEG, free CLT, and MPDA-PEG-CLT nanospheres were added to 143B cells and the therapeutic effect was determined after 24 h of direct incubation.

Live/Dead Cell Viability Assay

143B cells were cultured with MSCs cells in 24-well plates for 12 h, in which CLT, MPDA-PEG, and MPDA-PEG-CLT were added for 4 h, and then the MPDA-PEG + Laser and MPDA-PEG- CLT + Laser groups were irradiated for 5 min under 808 nm laser irradiation. Following this, cells were stained with calcein-am and propidium iodide (PI) for 15 min. Images of cellular fluorescence were taken using an inverted fluorescence microscope.

Cell Cycle and Apoptosis Assays

Cells were seeded into 6-well plates and co-incubated with CLT, MPDA-PEG, and MPDA-PEG-CLT for 4 h. Then the MPDA-PEG + Laser and MPDA-PEG- CLT + Laser groups were irradiated for 5 min under 808 nm laser irradiation and placed in a cell incubator for 24 h. Cells used for cell cycle analysis were digested with trypsin (Hyclone), washed twice with phosphate buffered saline (PBS), and fixed in 70% ethanol overnight at 4 ° C. Cells were centrifuged at 500 g for 5 min, washed twice with cold PBS, and centrifuged. Cell cycle analysis was performed by fluorescence-activated cell sorting after treatment with RNase A (0.1 mg/mL) and staining with propidium iodide (PI, 0.05 mg/mL; 4A Biotech

Beijing, China) for 30 min at 37 ° C. For analysis of apoptosis, cells were trypsinized followed by two PBS washing steps. Cells were stained using Annexin V/PI assay kit (4A Biotech, Beijing, China) for 5 min at room temperature. Apoptotic cells were determined using a flow cytometer (Beckman Coulter). All experiments were repeated at least three times.

Mitochondrial Membrane Potential and Apoptosis Detection

143B cells were cultured in 24-well plates for 12 h, in which CLT, MPDA-PEG, and MPDA-PEG-CLT were added for co-incubation for 4 h, and then the MPDA-PEG + Laser and MPDA-PEG-CLT + Laser groups were irradiated for 5 min under 808 nm laser irradiation. Following this, they were placed in a cell incubator for an additional 12 hours. Then, the changes of mitochondrial membrane potential and apoptosis in each group were detected by mitochondrial membrane potential and apoptosis detection kit.

Western Blotting

Protein samples were extracted using cell lysis buffer (P0013, Beyotime, Shanghai, China) supplemented with proteinase (04693159001, Roche, Switzerland) and phosphatase inhibitors (4906837001, Roche). Then, 1/5 volume of loading buffer was added into the cell lysis at 100 °C for 10 min. Protein samples were separated by sodium dodecyl sulfate polyacrylamide gel electrophoresis and then transferred onto polyvinylidene fluoride membranes. Blots were blocked in 5% bovine serum albumin for 2 h at 25 °C, then incubate the membrane with specific antibodies against Caspase 3 (Affinity,1:1000, #AF7022), Caspase 9(Affinity,1:1000, #AF5240), Bax (Affinity,1:1000, #AF0120) and Bcl-2 (Affinity,1:1000, #AF6139) at 4 °C overnight. Blots were incubated with a secondary antibody conjugated to horseradish peroxidase (Bioss, 1:5000, #bs-0295G) for 2 h at 25 °C. Finally, each membrane was exposed to ECL (SQ202, Epizyme, Shanghai, China).

Immunofluorescence Detection of Mitochondrial Apoptosis in Osteosarcoma Cells

143B cells were cultured in 24-well plates for 12 h, in which CLT, MPDA-PEG, and MPDA-PEG-CLT were added for co-incubation for 4 h, and then the MPDA-PEG + Laser and MPDA-PEG- CLT + Laser groups were irradiated for 5 min under 808 nm laser irradiation. Cells were then washed three times with phosphate-buffered saline (PBS) and fixed in 4% paraformaldehyde for 15 min. Following three additional PBS washes, 0.5% Triton X-100 (in PBS) was used for 20 min at room temperature. Goat serum was blocked for 30 minutes after three additional PBS washes and then incubated overnight at 4°C with Cytochrome C (HUABIO, 1:100, M1701-9) and Tomo20 (Cell Signaling Technology, 1:100, 42406) antibodies. Fluorescent secondary antibodies (Alexa Fluor ® 488 Conjugate (Cell Signaling Technology, 1:100, 4408S), Alexa Fluor ® 594 Conjugate (Cell Signaling Technology, 1:100, 8889S)) were instilled after 3 washes with TBST the following day and incubated for 1 hour at room temperature in a humidified chamber. After washing three times again with TBST, cells were stained with DAPI for 15 min before taking fluorescence images of the cells using a confocal laser scanning microscope.

Extraction and Culture of Bone Marrow Stromal Cells

Primary BMSCs were extracted and cultured as described[22] and cultured in α-MEM containing 10% fetal bovine serum (ExCell Bio, China). The medium was changed in half every 2 to 3 days. BMSC were passaged once on day 7 or 8 after inoculation, and cells were re-inoculated at 1.5×10^5 cells/cm^2 for osteoblast differentiation experiments.

Osteoblast Differentiation Assays

Alkaline phosphatase (AP) activity and expression were examined for osteoblast differentiation and, in brief, BMSCs were replated overnight in 24-well plates. The following day, cells were treated with celastrol (0.4 μM) for three days. AP staining assay was performed using the BCIP/NBT alkaline phosphatase chromogen kit. Quantitative real-time PCR (qPCR) was performed to detect osteoblast marker gene expression.

Mineralization Assay

Bone nodule formation was tested as previously described.[23] Briefly, cells were grown to confluence in complete growth medium and cultured in osteogenic medium containing 50 mg/L ascorbic acid and 10 mM sodium β-glycerophosphate for 14 days. Bone nodule formation was observed microscopically and mineralization was detected and quantified by Alizarin Red S staining, and mineralization was quantified by absorbance assay after de-staining using pure water.

Quantitative PCR

Total RNA was extracted following treatment of cells using Trizol (Invitrogen, CA, USA). cDNA was synthesized from extracted total RNA by reverse transcription reaction kit instructions (TAKARA, Japan). Synthesized cDNAs were diluted 5-fold and kept at −20 ° C until used as templates and primer sets for qPCR (Table 1). Relative mRNA expression levels of the housekeeping gene Gapdh were normalized using the $2^{-\Delta\Delta CT}$ method.

In vivo Treatment

143B cell line was inoculated subcutaneously into nude mice to prepare a subcutaneous osteosarcoma tumor model, and 100 μL of CY5-modified MPDA-PEG nanoparticle suspension (4 mg mL^{-1}) was injected into the tail vein to photograph the targeted aggregation effect of MPDA-PEG nanospheres in nude mice at different time periods using a small animal fluorescent intravital imager.

When the tumor volume reached 80 mm3, mice were divided into 6 groups (n=5): control group, CLT group, MPDA-PEG-CLT group, MPDA-PEG + 2 w cm^{-2} laser group, and MPDA-PEG-CLT + 2 w cm^{-2} laser group. Mice in the CLT group received 100 μL (0.6 mg mL − 1) of free CLT intravenously. Mice in the MPDA-PEG-CLT, MPDA-PEG + 2w cm^{-2} laser, and MPDA-PEG-CLT + 2w cm^{-2} laser groups were injected intravenously with 100 μL of MPDA-PEG /MPDA-PEG-CLT nanoparticle suspension (4 mg mL^{-1}). Tumors were exposed to an 808 nm NIR laser 4 hours after injection. Temperature at the tumor site was recorded with an infrared camera. Tumor size and mouse weight were measured every other day. On the 14th day, the mice were sacrificed, and the tumors and main organs (heart, liver, lung, and kidney) were dissected and stained with hematoxylin and eosin (HampE) for histological analysis.

Statistical Analysis

All data in this paper are expressed as mean result ± SD. Unpaired student's *t* -test was used for comparison between two testing groups and a probability (P) less than 0.05 was considered statistical significance.

Results and Discussion

Preparation and Characterization of MPDA-PEG

MPDA nanospheres with mesoporous structures were prepared by adopting and modifying the reported emulsion-induced interface assembly method.[20,21] Scanning electron microscopy (SEM) and transmission electron microscopy (TEM) images are shown in Figure 1A and B. The particle size distribution of MPDA nanospheres is uniform, the mesopores are arranged radially, and the main components are composed of C, N, and O elements (Figure 1C). TEM images show that the mesopore size of MPDA is ~15-20nm.

Table 1 Sequences of Primers Used for qRT-PCR (Mouse)

Primer	Forward	Reverse
GAPDH	GCACAGTCAAGGCCGAGAAT	GCCTTCTCCATGGTGGTGAA
Alp	ACACCAATGTAGCCAAGAATGTCA	GATTCGGGCAGCGGTTACT
Runx2	CCGGTCTCCTTCCAGGAT	GGGAACTGCTGTGGCTTC
Col1	GAGCGGAGAGTACTGGATCG	GCTTCTTTTCCTTGGGGTTC

https://doi.org/10.2147/IJN.S527094

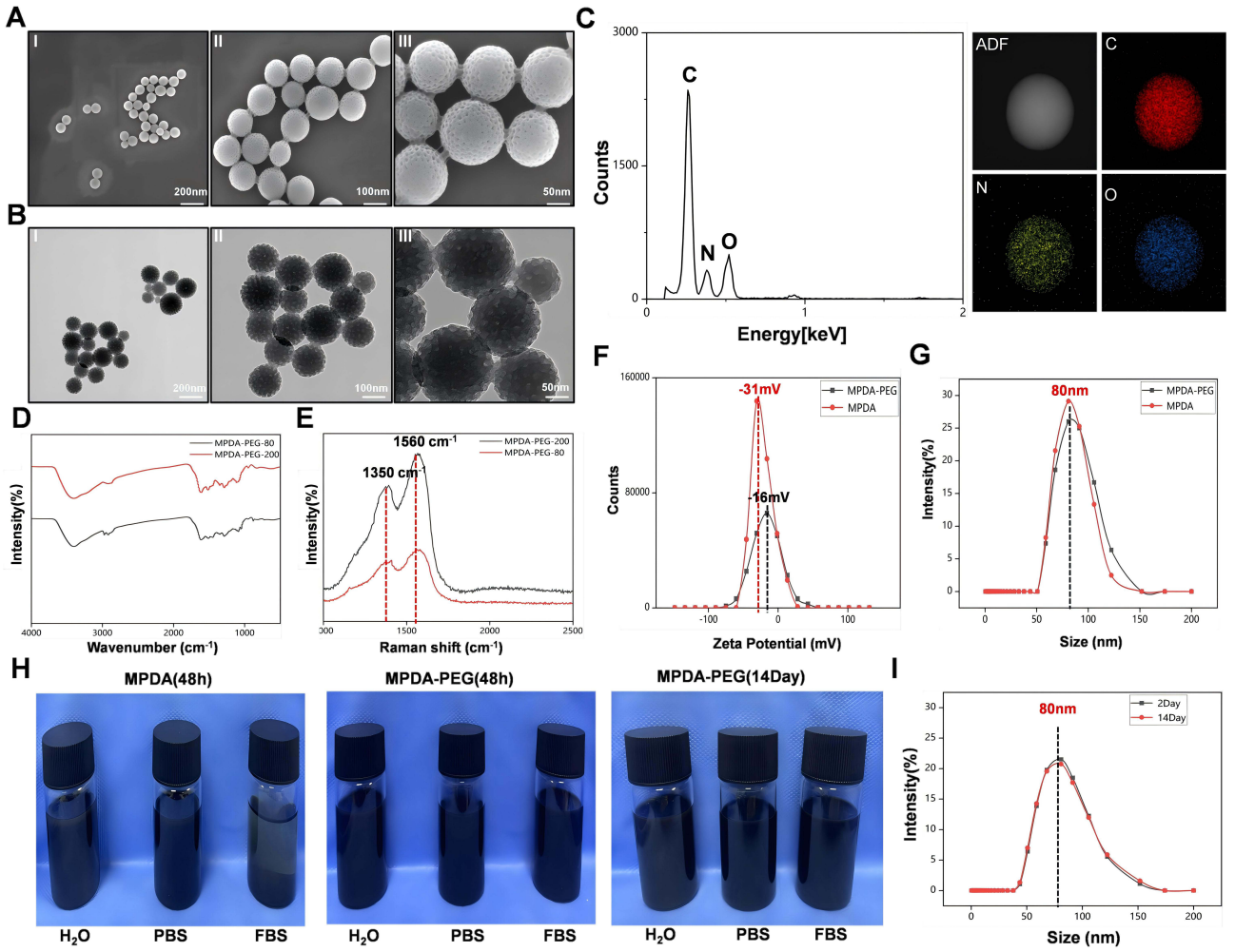

Figure 1 Characterization of MPDA nanoparticles. (**A**) SEM images of MPDA nanoparticles, ~ 80 nm: (i) scale bar at 200 nm, (ii) scale bar at 100 nm and (iii) scale bar at 50 nm. (**B**)TEM images of MPDA nanoparticles, ~ 80 nm: (i) scale bar at 200 nm, (ii) scale bar at 100 nm) and (iii) scale bar at 50 nm. (**C**) Elemental analysis profile of MPDA nanoparticles. (**D**) FT-IR spectra of MPDA-PEG nanoparticles of different sizes. (**E**) Raman spectra of MPDA-PEG nanoparticles of different sizes. (**F**) Zeta potential of MPDA nanoparticles before and after PEG modification. (**G**) Particle size of MPDA nanoparticles before and after PEG modification. (**H**) Biostability of MPDA nanoparticles in different media for different time periods before and after PEG modification. (**I**) Particle size of MPDA-PEG nanoparticles treated in physiological medium (FBS) for 2 and 14 days.

MPDA-PEG nanospheres with different diameters were then characterized by Fourier transform infrared spectroscopy (FT-IR) and Raman spectroscopy. The FT-IR spectrum is shown in Figure 1D, with peaks around 3400 cm^{-1} attributed to stretching vibrations of N-H and O-H hydroxyl groups, and a clear peak at 1616 cm^{-1} is stretching vibration of C = C double bond of aromatic ring.[24] These functional groups endow the MPDA-PEG nanospheres with active surface modification. As shown in Figure 1E, Raman spectroscopy was used to provide information on the disordered and defective structure of MPDA-PEG nanospheres. Two strong peaks centered at 1350 and 1560 cm^{-1} were observed, and the vibration signal at 1350 cm^{-1} was attributed to the sp2 carbon of the 2D hexagonal structure lattice (D-band) while the vibration signal at 1560 cm^{-1} corresponded to the sp2 carbon of the aromatic structure ring (G-band) in plane.[25] This indicates that the obtained mesoporous polydopamine nanospheres may have a high-density vacancy structure.

In order to enhance the stability and dispersibility of MPDA in physiological media and achieve the purpose of applying it to organisms in the future, MPDA was functionalized with PEG using NH2·PEG under alkaline conditions (pH 12.0) through Michael addition/Schiff base reaction. As shown in Figure 1F, the Zeta potential of PEG-modified MPDA (MPDA-PEG) nanospheres changed from −31mV to −16mV, proving that PEG was successfully modified on the surface of MPDA nanospheres, which helps to prolong the circulation time of loaded drugs. As shown in Figure 1G, the particle size of the modified MPDA-PEG nanospheres and MPDA nanospheres did not change much (~80nm). In

addition, as shown in Figure 1H, PEG-modified MPDA nanospheres showed good stability in physiological medium (FBS) for a long time (~ 14 days); in addition, PEG-modified MPDA nanospheres treated in FBS for different times were tested for particle size, and it was found that the particle size of MPDA nanospheres treated for 2 days and 14 days did not change much (Figure 1I), which indicated that PEG-modified MPDA nanospheres had good long-term stability in physiological medium (FBS) and would be conducive to further biological applications.

Photothermal Effect of MPDA-PEG

In recent years, nanomaterials with high NIR absorption and photothermal conversion efficiency have been widely used in PTT.[26] In this study, to investigate the photothermal effect of MPDA-PEG nanospheres, we synthesized PEG-modified MPDA nanospheres (approximately 80 and 200 nm in diameter, defined as MPDA-PEG-80 and MPDA-PEG -200, respectively) for comparison (TEM images are shown in Figure 1B, and FT-IR and Raman spectra are shown in Figure 1D and E). Then, MPDA-PEG (100 μg mL $^{-1}$) was irradiated with a near-infrared laser at 808 nm, 2 W cm^{-2} for 5 min, and temperature changes were recorded using an infrared thermal imager. As shown in Figure 2A and B, MPDAPEG-200 nanospheres could increase the temperature from 18 ° C to 66.5 ° C (ΔT = 48.5 °C), while MPDA-PEG-80 nanospheres increased the temperature from 18 ° C to 42.5 ° C (ΔT = 24.5 °C). In addition, MPDA-PEG had a better photothermal effect compared to PBS (Figure 2C). The above results showed that MPDA-PEG nanospheres had enhanced photothermal effects with increasing size, but in tumor hyperthermia applications, the intratumor temperature is generally controlled at 39.5–45.0°C, which is more likely to cause cell necrosis.[27] Temperature may be reduced appropriately in combination with other antineoplastic therapy. When the temperature exceeds 45°C, the normal tissue cells in the body will also be damaged. In summary, we selected MPDA-PEG-80 nanospheres for the next study.

In order to detect the excellent photothermal effect of MPDAPEG-190, the photothermal stability of MPDA-PEG nanospheres was first examined by repeated exposure to near-infrared laser irradiation (808 nm, 2 W cm^{-2}) for three cycles. Almost no loss in thermal fatigue resistance was observed during the 3 NIR laser exposure cycles (Figure 2D). Secondly, we calculated the photothermal conversion efficiency (η) of MPDA-PEG nanospheres, and as shown in Figure 2E, the η value of MPDA-PEG was 37.6%. In addition, MPDA-PEG nanospheres were thus demonstrated to have good photothermal stability.

Tumor tissue is in an acidic microenvironment with excessive hydrogen peroxide,[28] and H_2O_2 is also widely distributed in macrophages and major organs.[29] Therefore, the biodegradability of MPDA-PEG nanospheres was studied in the presence of hydrogen peroxide. The results showed that the absorption of MPDA-PEG at 808nm decreased with the extension of reaction time and the increase of H_2O_2 concentration (Figure 2F and G). These results indicate that MPDA-PEG nanospheres have good biodegradability.

Celastrol Loading and Release

Due to the poor water solubility of celastrol, significant organ toxicity with poor intestinal permeability, its application is limited.[6,30,31] MPDA-PEG has mesoporous structure and is an ideal drug delivery carrier for celastrol, which can solve the in vivo toxicity caused by the inability of celastrol to target tumors.

Therefore, we investigated the celastrol loading capacity of MPDA-PEG-190 nanospheres. As shown in Figure 3A, the successful loading of celastrol was confirmed by FT-IR spectroscopy. Celastrol spectra showed characteristic absorptions at 1718 and 1244 cm^{-1}, which were attributed to symmetric or asymmetric stretching of C=O and C-O, respectively. After celastrol was loaded into MPDA-PEG particles, the new peaks were located at 1718 cm^{-1} and 1244 cm^{-1}, confirming that celastrol had loaded into MPDA-PEG. Nitrogen adsorption-desorption isotherm experiments of MPDA-PEG and celastrol-loaded MPDA-PEG (MPDA-PEG-CLT) nanospheres (Figure 3B and C) showed that the specific surface area and pore volume of MPDA-PEG nanospheres decreased from 286 m^2 g^{-1} and 0.32 cm^3 g^{-1} to 44 m^2 g^{-1} and 0.12 cm^3 g^{-1}, respectively, due to successful loading of celastrol into the mesoporous channel of MPDA-PEG nanospheres. Subsequently, the encapsulation efficiency and drug loading rate of MPDA-PEG nanospheres were further calculated. It was found that MPDA-PEG could effectively load celastrol molecule (DLC, 15%).

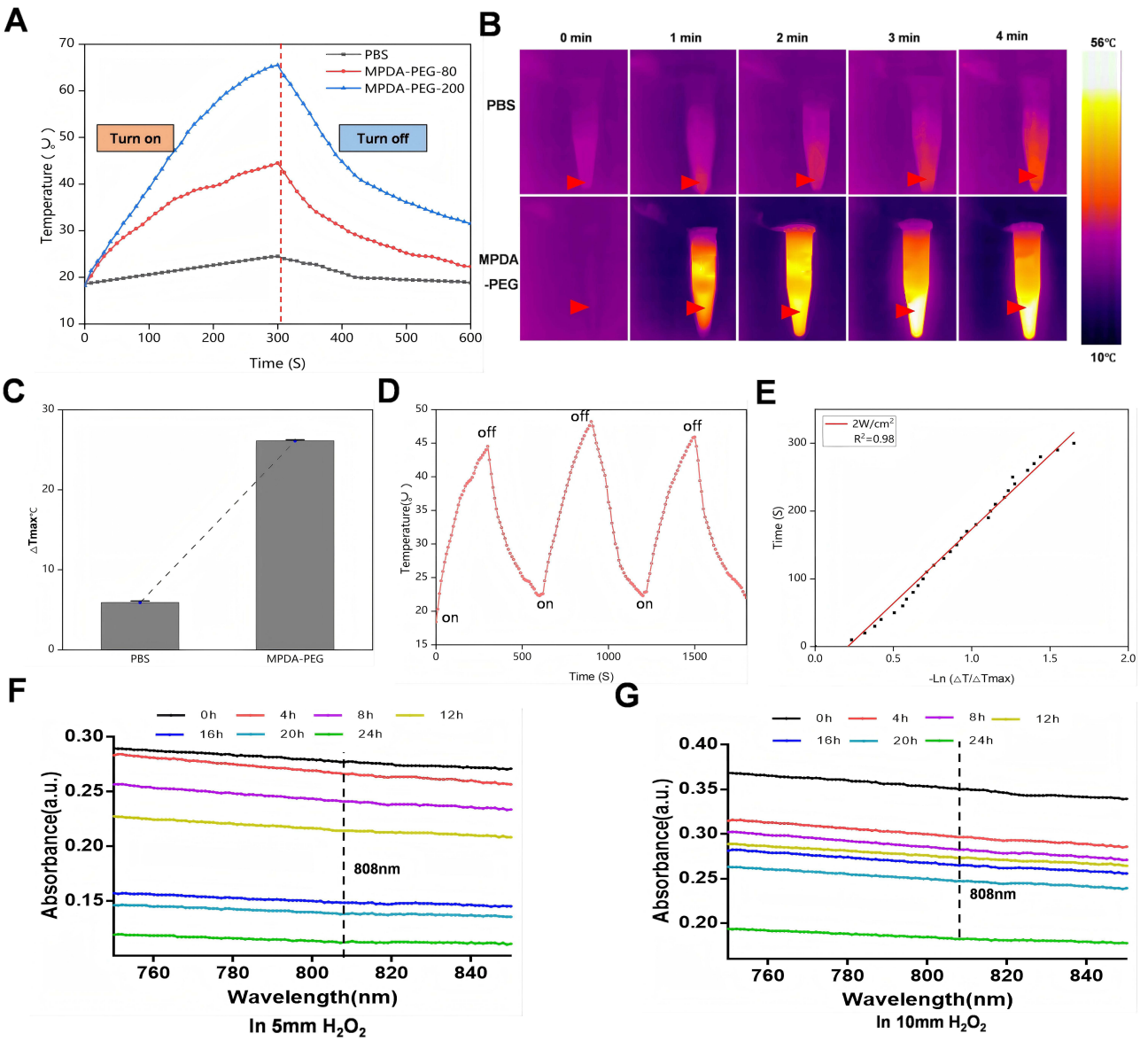

Figure 2 Determination of thermal conversion efficiency of MPDA nanoparticles. (**A**) Photothermal effect temperature change of MPDA-PEG nanoparticles irradiated with 808 nm laser for 5 min. (**B**) Infrared imaging of MPDA-PEG nanoparticles irradiated with 808 nm laser at different times (red arrows in the picture are indicated by the temperature measurement point). (**C**) Maximum temperature change of MPDA-PEG during NIR laser irradiation. (**D**) Temperature change of MPDA-PEG suspension (100 μg mL − 1) after 3 cycles of laser irradiation (808 nm, 2 W cm − 2). (**E**) -Ln (ΔT/ΔTmax) linear time data. (**F** and **G**) Degradation of MPDA-PEG nanoparticles in different concentrations of hydrogen peroxide (5 mm/10 mm).

Therefore, the mesoporous structure is able to significantly improve the anticancer drug loading (DLC) of MPDA-PEG.

Next, we evaluated the release behavior of celastrol from MPDA-PEG-CLT nanospheres. The results showed that MPDA-PEG-CLT nanospheres released about 18% of celastrol within 24 hours (Figure 3D). This result suggested that MPDA-PEG nanospheres can prevent premature and excessive release of celastrol molecules, thereby achieving a sustained in vivo release effect. To further understand the effect of NIR irradiation on the release properties of celastrol, we irradiated MPDA-PEG-CLT nanoparticle dispersions with 808 nm laser (2 W cm^{-2}, 5 min) at 2-hour intervals. As shown in Figure 3D, the MPDA-PEG-CLT nanospheres finally released nearly 86% of free celastrol molecules. The drastic release of celastrol is mainly due to a rapid increase in temperature under NIR radiation which leads to its escape from the mesoporous channel of MPDA-PEG nanospheres.[32]

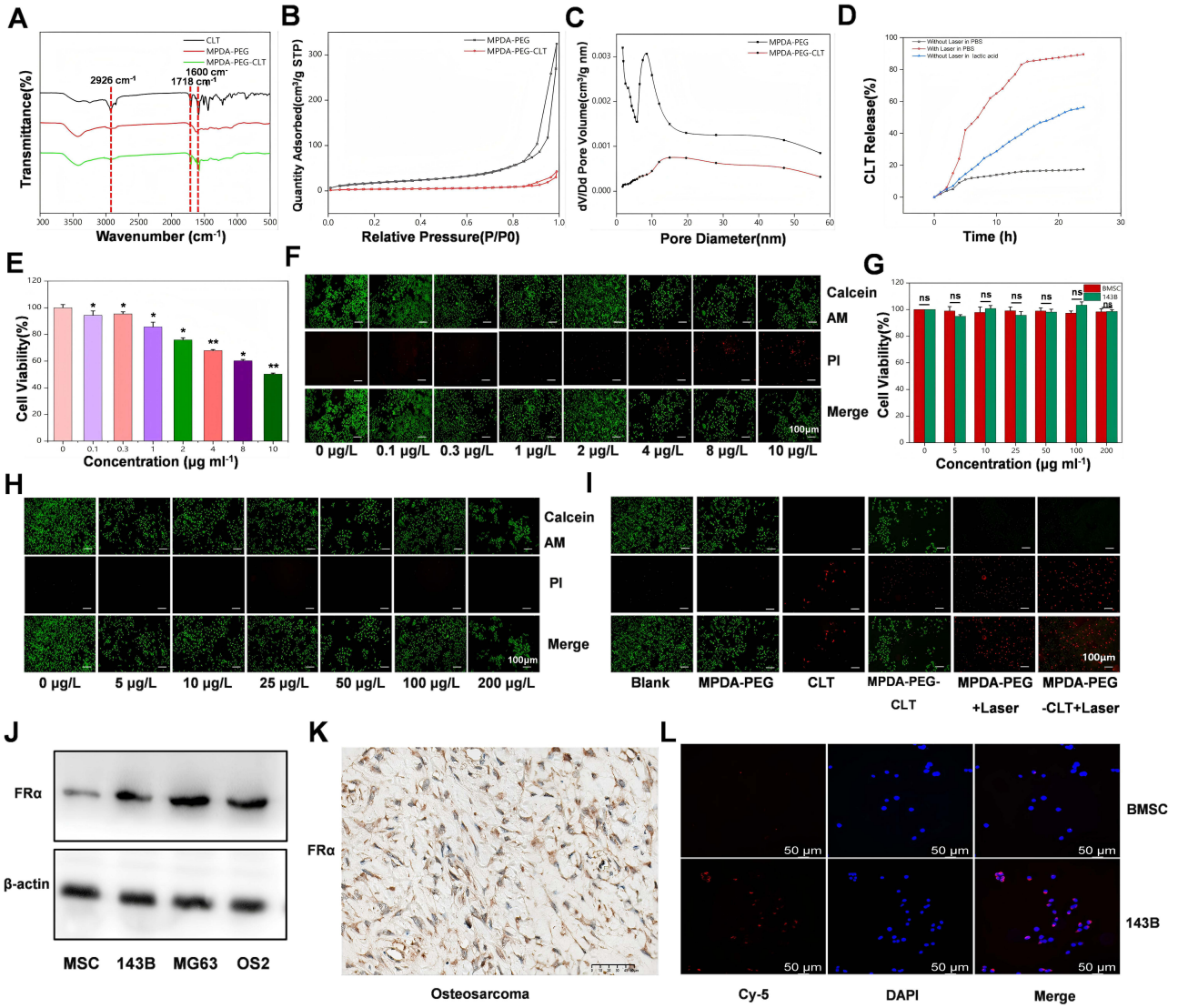

Figure 3 Determination of Drug Loading and Biological Application of MPDA-PEG-CLT Nanoparticles. (**A**) FT-IR spectra of CLT, MPDA-PEG and CLT-loaded MPDA-PEG nanoparticles. (**B**) Nitrogen adsorption-desorption isotherms and (**C**) pore size distribution curves of MPDA-PEG and CLT-loaded MPDA-PEG. (**D**) CLT release properties of MPDA-PEG-CLT with or without NIR irradiation (808 nm, 2 W cm − 2, 5 min) in different media for 2 h intervals. (**E**) Cell survival rate of 143B cells incubated with different concentrations of CLT for 24 h. (**F**) Images of 143B cells co-stained with calcein (green fluorescence, living cells) and propidium iodide (PI, red fluorescence, dead cells), green fluorescent precursor compounds incubated with different concentrations of CLT. (**G**) In vitro cytotoxicity of MPDA-PEG at various concentrations. Data are mean ± sd. N = 3. ns: No significant difference. (**H**) Images of 143B cells co-stained with calcein (green fluorescence, viable cells) and propidium iodide (PI, red fluorescence, dead cells), green fluorescent precursor compounds incubated with different concentrations of MPDA-PEG. Scale bar is 100 μm. $p < 0.05$, $p < 0.01$ compared to 0 μg/L group. (**I**) Images of calcein (green fluorescence, living cells) and propidium iodide (PI, red fluorescence, dead cells), green fluorescent precursors of 143B cells incubated with different nanoparticles. Scale bar is 100 μm. (**J**) WB was used to detect the protein expression of FRα in osteosarcoma cell lines; (**K**) immunohistochemistry was used to detect the expression of FRα in osteosarcoma tissues; (**L**) 143B cell-specific uptake of MPDA-PEG-CY5 fluorescence map with a scale bar of 100 μm.

The above results showed that MPDA-PEG-CLT exhibits NIR-responsive drug release behavior, and the increase in temperature could promote the release of chemotherapeutic drugs at the tumor site, increase the bioavailability of CLT, reduce side effects, and produce a synergistic therapeutic effect.[33,34]

Extracorporeal Chemo-Photothermal Therapy

Through previous studies, we found that MPDA-PEG nanospheres have excellent photothermal effect and excellent CLT loading and sustained release capabilities. Next, we further investigated its biological application value. First, the biocompatibility of MPDA-PEG and free CLT on 143B and BMSCs was determined by CCK-8 and live-dead staining assay. The results showed that cell viability decreased with increasing CLT concentration after incubation of 143B cells

https://doi.org/10.2147/IJN.S527094

with different concentrations of CLT (0.1–10 μg mL^{-1}) for 24 hours (Figure 3E and F). However, MPDA-PEG (5–200 μg mL^{-1}) was incubated with 143B cells and BMSCs cells for 24 hours. As shown in Figure 3G and H, the cell survival rate was above 95% in all groups even at high concentration (200 μg mL^{-1}), indicating good biocompatibility of MPDA-PEG.

To further investigate the synergistic therapeutic effect of MPDA-PEG-CLT nanospheres with photothermal therapy, we incubated 143B cells using MPDA-PEG, free CLT, and MPDA-PEG-CLT, MPDA-PEG + 2 w cm^{-2} laser, and MPDA-PEG-CLT + 2 w cm^{-2} laser, respectively. As shown in Figure 3I, the survival rate of cells incubated with blank control and MPDA-PEG was more than 95%, indicating that blank MPDA-PEG had little harm to cancer cells. However, compared with free CLT, the cytotoxicity of MPDA-PEG-CLT group was significantly reduced, which may be related to the sustained release of MPDA-PEG-CLT and significantly improved the toxic side effects caused by free CLT. However, the treatment effect was more obvious in the MPDA-PEG + 2 w cm^{-2} laser group as well as the MPDA-PEG-CLT + 2 w cm^{-2} laser group, and almost all 143B cells died. In summary, MPDA-PEG-CLT nanospheres have a good synergistic therapeutic effect with near-infrared hyperthermia.

In addition, the specific targeting of MPDA-PEG-CLT nanospheres to osteosarcoma is essential for in vivo and in vitro treatment. Folate receptors have been found to be overexpressed in most tumors[35] and also play an important role in drug targeted delivery in osteosarcoma as a surface modifiers of nanomaterials.[36–38] Our experimental results also showed that folate receptor presented high expression in clinical samples of osteosarcoma as well as osteosarcoma cell lines (Figure 3J and K). Therefore, in the previous preparation of MPDA-PEG-CLT nanospheres, we used Fol-PEG-NH_2 to surface modify MPDA in order to achieve specific targeting of osteosarcoma cells. To verify whether MPDA-PEG-CLT nanospheres could be ingested by cells, we incubated 143B cells, BMSCs cells with Cy5-modified MPDA-PEG for 4 h to conduct cell uptake assay. The results showed that the red fluorescence signal emitted by MPDA-PEG-Cy5 could be observed in osteosarcoma 143B cells (Figure 3L), while the red fluorescence signal was significantly reduced in BMSCs cells. This indicated that MPDA-PEG-CLT could be effectively taken up by osteosarcoma cells.

MPDA-PEG-CLT Leads to Mitochondrial Dysfunction in Osteosarcoma Cells

Studies have shown that celastrol has good antitumor effects and inhibits the progression of a variety of tumors including glioma, leukemia, melanoma, pancreatic cancer, lung cancer, prostate cancer, breast cancer, and colorectal cancer. The specific mechanism are mainly manifested in the following aspects: it can cause mitochondrial dysfunction and enhance glycolysis, thereby inducing tumor cell death; it can regulate the metastasis of liver cancer cells by inhibiting the phosphorylation of Thr567 at the linker protein ezrin between the cytoskeleton and the cell membrane mediated by protein serine/threonine kinase (ROCK2); and it plays an anti-tumor role by regulating the PI3K/AKT pathway, NFκB signaling pathway], and MAPK signaling pathway.

We found that MPDA-PEG-CLT could arrest the cell cycle of osteosarcoma cells in G2/S phase after incubation with osteosarcoma cells (Figure 4A and B), and MPDA-PEG-CLT could also promote osteosarcoma cell apoptosis (Figure 4C and D), but the cell cycle arrest and the number of apoptotic cells induced by MPDA-PEG-CLT treatment group were decreased compared with the free CLT group, consistent with the previous results, which may be caused by the slow and continuous release of MPDA-PEG-CLT. It has been found that mitochondria undergo remodeling of mitochondrial structure and increased outer membrane permeability during apoptosis, and Cyt C is involved in the process of apoptosis by releasing irreversible activation of downstream caspases proteins.[39] Next, we examined the effect of MPDA-PEG-CLT on mitochondrial function in osteosarcoma cells. It was found that MPDA-PEG-CLT was able to enhance mitochondrial outer mode permeability (Figure 4E) and decrease mitochondrial membrane potential (Figure 4F) in 143B cells. In addition, we found that MPDA-PEG-CLT treatment of 143B cells enhanced Caspases 3, Caspases 9 protein expression levels, increased protein expression levels of pro-apoptotic protein Bax and decreased protein expression levels of anti-apoptotic protein Bcl2 (Figure 4G). In the meantime, MPDA-PEG-CLT treatment of 143B cells also promoted cytochrome c (Cytochrome C) release from mitochondria to the cytoplasm (Figure 4H). Taken together, our results demonstrate that MPDA-PEG-CLT can regulate osteosarcoma fate by promoting mitochondrial apoptosis in osteosarcoma cells.

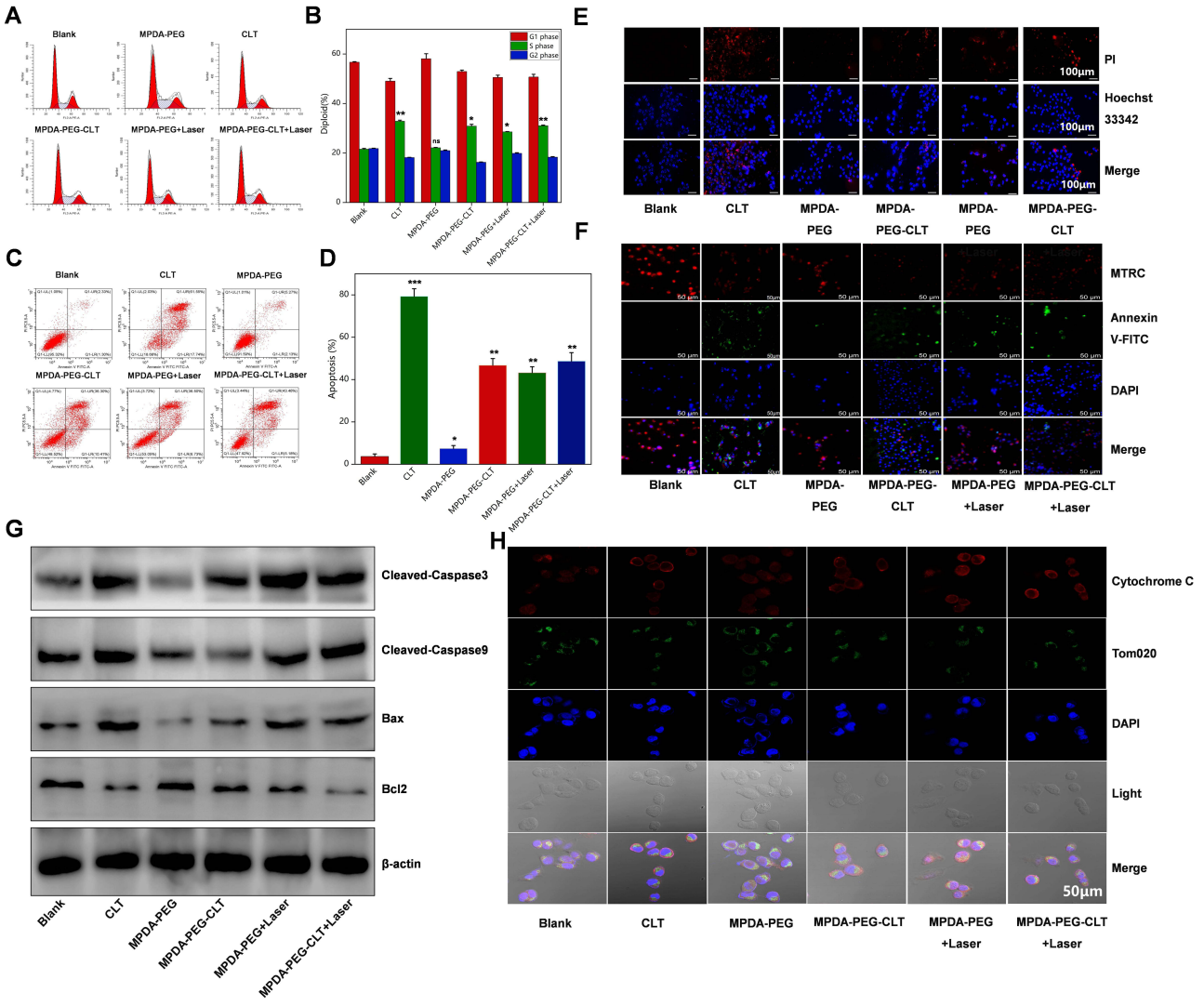

Figure 4 Effect of different treatment groups on osteosarcoma cell function. (**A**) Cell cycle detection by flow cytometry after incubation of 143B cells with MPDA-PEG, CLT, MPDA-PEG-CLT, MPDA-PEG + Laser, MPDA-PEG-CLT + Laser, MPDA-PEG-CLT + Laser and (**B**) Results statistics. Figure A red areas: G0/G1 and G2 phase; Figure A shadow areas: S phase.(**C**) Apoptosis detection by flow cytometry after incubation of 143B cells with MPDA-PEG, CLT, MPDA-PEG-CLT, MPDA-PEG + laser, MPDA-PEG-CLT + laser, MPDA-PEG-CLT + laser, and MPDA-PEG-CLT + laser. (**D**) Results statistics. * $p < 0.05$. ** $p < 0.01$. *** $p < 0.001$. VS Blank group.ns: No significant difference. (**E**) Fluorescence pattern of propidium iodide (PI, red fluorescence) staining after incubation of 143B cells with MPDA-PEG, CLT, MPDA-PEG-CLT, MPDA-PEG + Laser, MPDA-PEG-CLT + Laser, MPDA-PEG-CLT + Laser. The scale bar is 50μm. (**F**) Fluorescence maps of mitochondrial membrane potential (Mito Tracker Red CMXRos) and apoptosis (Annexin V-FITC) staining after incubation of 143B cells with MPDA-PEG, CLT, MPDA-PEG-CLT, MPDA-PEG + Laser, MPDA-PEG-CLT + Laser. The scale bar is 50μm.(**G**) WB was used to detect the protein expression of caspase3, caspase9, BAX, and Bcl2 in each group after MPDA-PEG, CLT, MPDA-PEG-CLT, MPDA-PEG + Laser, MPDA-PEG-CLT + Laser treatment of 143B cells with MPDA-PEG, CLT, MPDA-PEG-CLT + Laser, MPDA-PEG-CLT + Laser. (**H**) Immunofluorescence was used to detect the localization of Cytochrome C in each group after treatment of 143B cells with MPDA-PEG, CLT, MPDA-PEG-CLT, MPDA-PEG + Laser, MPDA-PEG-CLT + Laser, and MPDA-PEG-CLT + Laser. The scale bar is 50μm.

MPDA-PEG-CLT Promotes Osteogenic Differentiation of BMSCs

Bone defects caused by osteosarcoma erosion and surgical intervention are inevitable, making it difficult for the body to complete self-repair, and bringing persistent severe pain and lifelong disability to patients. The commonly used clinical treatment is bone transplantation and inorganic material filling, but due to the limited source of bone graft and the insufficient biological activity of inert material, repair failure and revision problems exist for a long time, it is urgent to remodel the bone tissue microenvironment in the lesion area in order to promote bone repair after osteosarcoma surgery. Therefore, we preliminarily investigated the mechanisms involved in the regulation of developmental differentiation of BMSC by MPDA-PEG-CLT.

https://doi.org/10.2147/IJN.S527094

It has been found that CLT has an inhibitory effect on lipid accumulation and adipogenesis in human adipose-derived stem cells (hADSCs).[40] In addition, CLT can also modulate the function of bone marrow-derived endothelial progenitor cells (BM-EPCs).[41] Moreover, CLT regulates the differentiation of bm-mscs by activating the AMPK/SIRT1-PGC-1α signaling pathway, and in addition, celastrol attenuates bone loss and bone marrow adipose tissue (MAT) accumulation in ovariectomized (OVX) and aged mice.[8]

Consistent with previous reports, MPDA-PEG-CLT promoted osteogenic differentiation of BMSCs, as shown by increasing osteoblast-specific alkaline phosphatase (AP) activity in BMSCs (Figure 5A), upregulating expression of osteoblast marker genes Alpl, Col1α1, Runx2, and Sp7 (Figure 5B), and increasing alizarin red-stained bone nodule formation (Figure 5C). These results suggest that CLT can regulate the bone tissue microenvironment, promote osteogenic differentiation of BMSCs, enhance the body ‘s own repair function, and improve the bone defect caused by osteosarcoma.

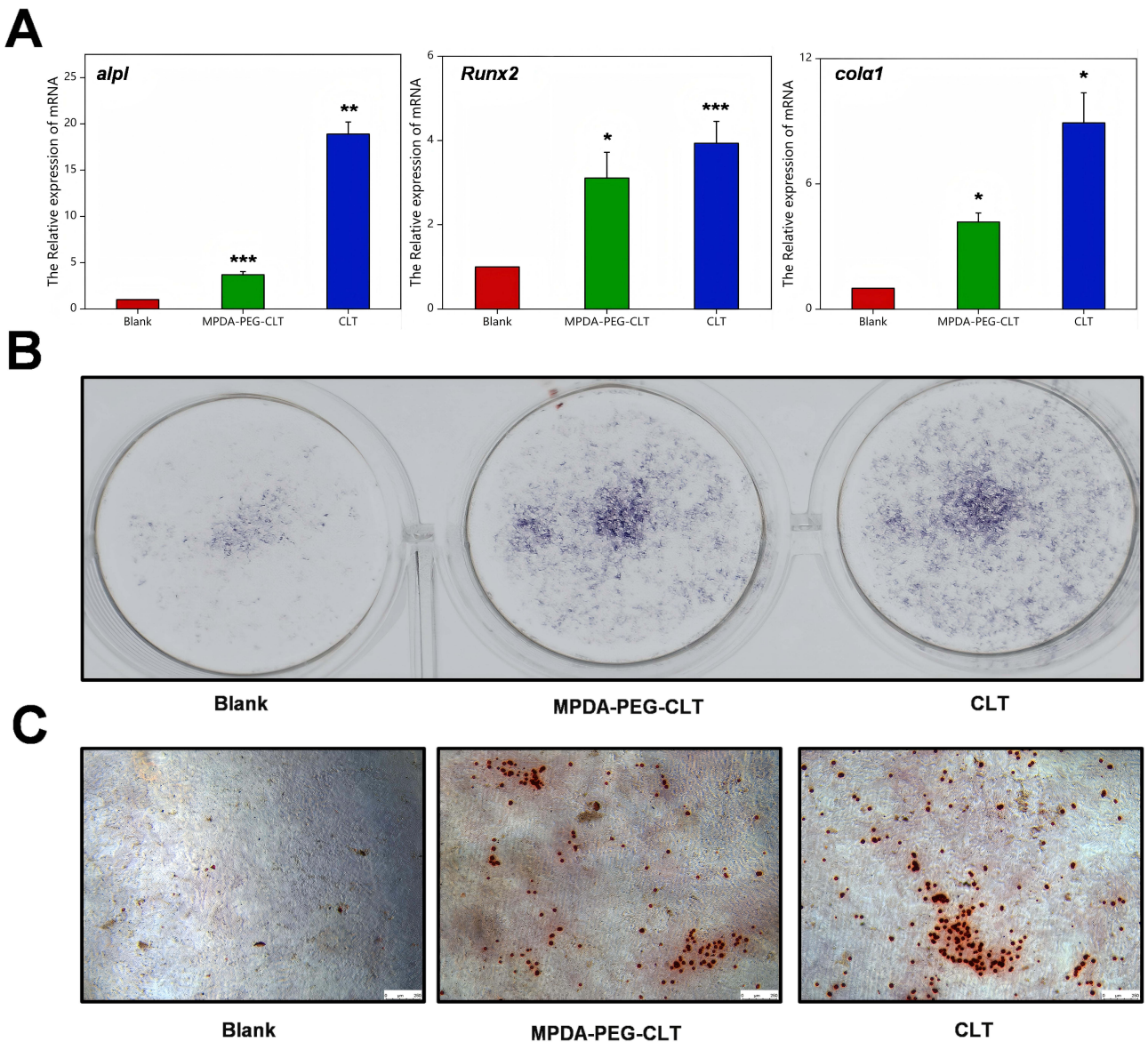

Figure 5 Effect of MPDA-PEG-CLT on osteogenic differentiation of BMSCs. (**A**) Expression levels of osteogenesis-related genes (ALP, Runx2, colα1) in MPDA-PEG-CLT as well as CLT-treated BMSC. Osteogenic differentiation ability was evaluated by (**B**) ALP staining and (**C**) Alizarin red staining. *$p < 0.05$. **$p < 0.01$. ***$p < 0.001$. The scale bar is 50μm.

In vivo Chemo-Photothermal Therapy

Subsequently, we further investigated the photothermal effect of MPDA-PEG on tumor-bearing mice. First, we injected 143B tumor-bearing mice (n=3) with 100 μL of MPDA-PEG-CY5 dispersion (4 mg mL^{-1}) via the tail vein to investigate the distribution and targeting of MPDA-PEG-CLT nanospheres in mice, and performed in vivo fluorescence imaging of nude mice at 0 h, 4 h, 12 h, and 24 h after injection. As shown in Figure 6A, the MPDA-PEG-CY5 nanospheres fluorescence signal began to concentrate at the tumor location in nude mice at 4 hours after injection and peaked at 24 hours, indicating that MPDA-PEG was able to enrich in the tumor area with time. In addition, 143B tumor-bearing mice were randomly divided into 2 groups of 3 mice each and injected with 100 μL MPDA-PEG-CLT dispersion (4 mg mL^{-1}) per mouse and PBS in the control group. Tumor areas were completely exposed to 808 nm laser light (2 W cm^{-2}) for 5 min at 6 h post-injection. The changes in tumor temperature were monitored using an infrared camera. As shown in Figure 6B, after 5 min of irradiation, tumor temperature rapidly increased from 28.6 °C to 46.7 °C (ΔT = 18.1 °C) in mice injected with MPDA-PEG-CLT, as compared with PBS-treated controls that did not increase by more than 8 °C after laser irradiation.

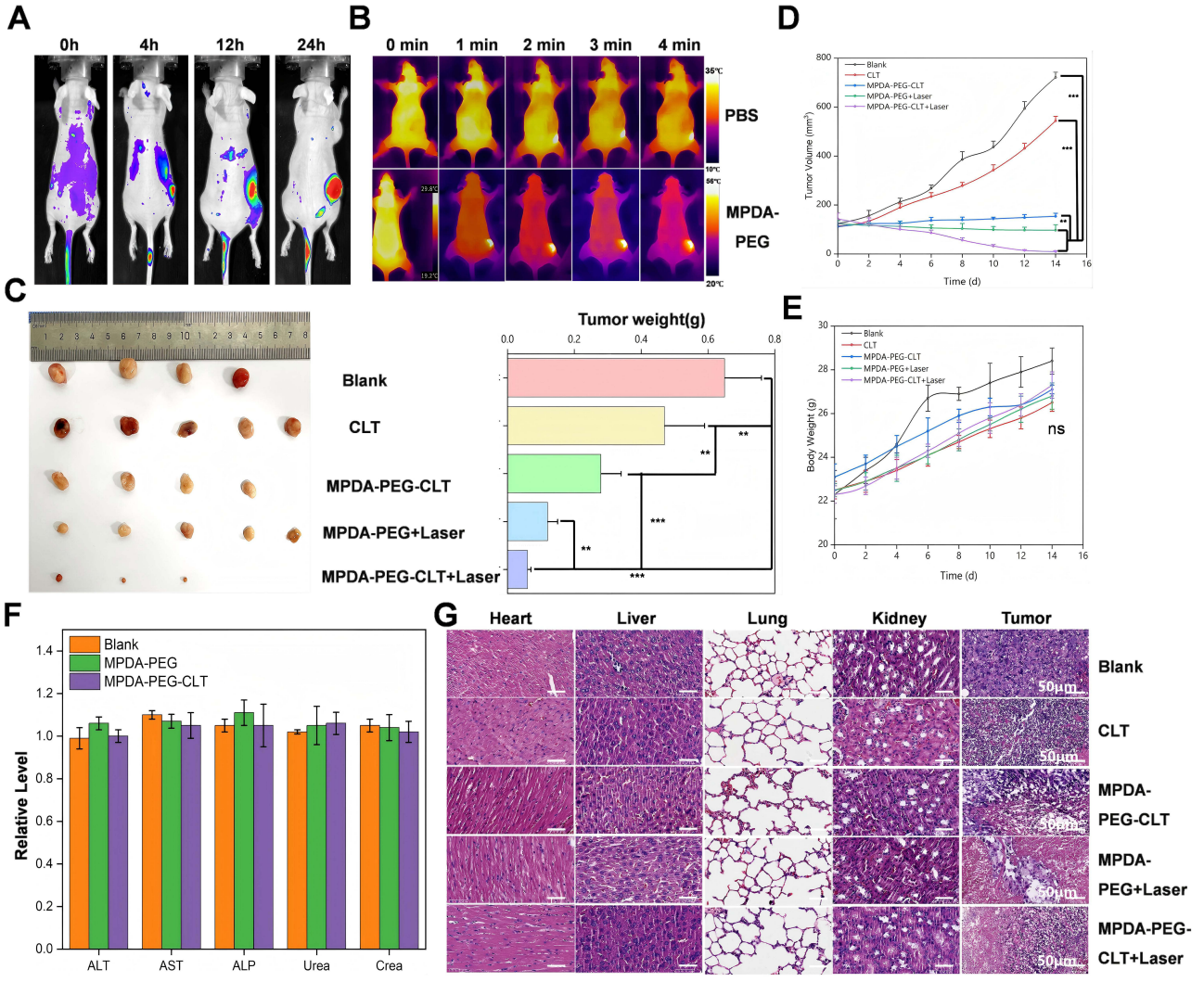

Figure 6 In Vivo Therapeutic Efficacy Assessment of MPDA-PEG-CLT. Fluorescence in vivo imaging (**A**) and regional temperature infrared imaging (**B**) of the tumor area were recorded at different time points after intravenous injection of MPDA-PEG- CLT nanoparticles. (**C**) Photos and weight of tumors dissected from each group on the 14th day after photothermal treatment. (**D**) Tumor volume curves of 143B tumor-bearing mice with different treatments. (**E**) Body weight curves of mice of each group. Data are means ± sd. N = 5. **p < 0.01, ***p < 0.001 and "ns" represents no significance. (**F**) Detection of liver function and renal function in mice of different treatment groups. (**G**) H&E staining images of major organs (heart, liver, lung, and kidney) and tumor tissues dissected from each group on the 14th day after photothermal treatment (40 X). The scale bars are 50 μm.

https://doi.org/10.2147/IJN.S527094

We have previously demonstrated that MPDA-PEG-CLT has good antitumor effects in vitro, and next we evaluated osteosarcoma therapeutic effects in mice. When the tumor volume of 143B tumor-bearing nude mice reached 80 mm^3, they were randomly divided into 6 groups of 5 mice each. Following a 4-hour suspension of MPDA-PEG-CLT particles injected via the tail vein, the tumor area was placed in 808 nm near-infrared light. As shown in Figure 6C, the control group showed rapid tumor growth. In comparison, tumor growth was decreased to different extents in the free CLT, MPDA-PEG-CLT, and MPDA-PEG + 2 W cm^{-2} laser groups (5 min). At the same time, irradiation of mice with MPDA-PEG-CLT + 2 W cm^{-2} laser for 5 min resulted in the highest degree of tumor ablation, and the therapeutic effect was the best, indicating that the synergistic treatment of PTT and celastrol was effective. In addition, the above results were consistent with the trend of tumor growth curves recorded (Figure 6D).

In addition, no significant weight loss was observed in any of the mouse groups (Figure 6E), and in addition, neither MPDA-PEG nor MPDA-PEG-CLT nanoparticles caused significant increases in liver and kidney parameters at 48 hours after injection compared with the control group (Figure 6F), suggesting that MPDA-PEG microspheres do not cause systemic toxicity. To further confirm the biocompatibility of MPDA-PEG nanospheres, mice were sacrificed and dissected on day 14 post-treatment for histological analysis of their tumors and major organs. As shown in Figure 6G, there was no significant organ damage and inflammation in each group compared with the control group, further verifying the safety and low toxicity of MPDA-PEG-CLT nanospheres. These results suggest that MPDA-PEG-CLT nanospheres can be used as an effective nanoplatform for chemo-photothermal therapy of tumors in vivo with relatively low systemic toxicity.

In summary, the MPDA-PEG delivery celastrol system prepared in this study has good safety and efficacy. In terms of drug loading capacity, MPDA achieves significantly higher drug loading (up to 15–20%) than liposomes, PLGA nanoparticles, or micelles by virtue of its mesoporous structure and π-π stacking and hydrophobic interactions with Cel, overcoming the bottleneck that the latter is often limited by the loading capacity of the material itself (usually < 5%).[42] At the same time, its stability benefits from the shielding effect of PEG, avoiding problems such as easy micelle dissociation and easy oxidative hydrolysis of liposomes, ensuring the integrity in blood circulation.[43] In terms of crucial drug release controllability, MPDA-PEG has inherent dual pH/NIR response release characteristics and can trigger drug release more accurately in the tumor microenvironment or cells, reduce off-target toxicity, and improve treatment efficiency compared with PLGA nanoparticles, gold nanoparticles, or unmodified MSNs, which mainly rely on passive diffusion drug release.[44] Regarding targeting, PEGylation confers its excellent "stealth" properties and long blood circulation time, laying the foundation for passive targeting (EPR effect), and its ease of modification also facilitates the attachment of targeting ligands to achieve active targeting, with comparable results but is usually easier and economical to prepare liposomes than antibody-modified liposomes.[45] In addition, a major highlight of MPDA-PEG is its inherent additional function, the efficient photothermal conversion ability, which allows it to achieve chemotherapy-photothermal synergistic therapy, while traditional single-loaded systems such as liposomes, PLGA, or common micelles usually require additional composite functional materials (eg, gold nanoparticles or magnetic particles) to achieve similar multifunctionalization.[46] Overall, MPDA-PEG as a novel nanocarrier has some advantages in delivering celastrol, but further studies are still needed to assess its transformability.

Conclusion

In summary, our study developed an MPDA-PEG nanodelivery system loaded with celastrol, which has the potential to be a new chemotherapeutic drug, for the chemo-photothermal synergistic treatment of osteosarcoma. The results showed that the MPDA-PEG nanospheres had good photothermal effect and excellent celastrol loading capacity. In addition, we verified that MPDA-PEG-CLT nanospheres have better therapeutic effect on osteosarcoma by in vitro and in vivo experiments, with less side effects and better therapeutic effect than single drug therapy and PTT therapy. Finally, we found that MPDA-PEG-CLT nanospheres could promote osteogenic differentiation of BMSCs in vitro, which may provide ideas for the application of MPDA-PEG-CLT nanospheres in the repair of bone defects caused by osteosarcoma invasion. Our study demonstrated that MPDA-PEG nanospheres are expected to play an important role in the synergistic treatment of osteosarcoma and bone defect repair with traditional Chinese medicine components such as celastrol as

novel chemotherapeutic drugs, and their good biocompatibility and degradability can reduce the adverse reactions of chemotherapeutic drugs in clinical treatment.

Ethical Statement

All animal experiments were conducted in accordance with the National Institutes of Health (NIH) Guide for the Care and Use of Laboratory Animals and approved by the Chongqing University Laboratory Animal Welfare Ethics Committee (Approval No.CQU20240306). Efforts were made to minimize animal suffering and reduce the number of animals used, following the ARRIVE guidelines (Animal Research: Reporting of In Vivo Experiments).

Author Contributions

All authors made a significant contribution to the work reported, whether that is in the conception, study design, execution, acquisition of data, analysis and interpretation, or in all these areas; took part in drafting, revising or critically reviewing the article; gave final approval of the version to be published; have agreed on the journal to which the article has been submitted; and agree to be accountable for all aspects of the work.

Funding

This work was supported by the Joint Funding Project of Chongqing Health Committee and Chongqing Science and Technology Bureau (2023MSXM034), and the Special Project for Technological Innovation and Applied Development of Chongqing Science and Technology Bureau (2022TIAD-KPX0243).

Disclosure

The authors declare that there are no conflicts of interest in this work. This article has been uploaded as a preprint to [https://www.researchgate.net/scientific-contributions/Yufei-Ma-2185677731] and [https://papers.ssrn.com/sol3/papers.cfm?abstract_id=5096737].

References

1. Barzegari A, Salemi F, Kamyab A, et al. The efficacy and applicability of chimeric antigen receptor (CAR) T cell-based regimens for primary bone tumors: a comprehensive review of current evidence. *J Bone Oncol*. 2024;48:100635. doi:10.1016/j.jbo.2024.100635
2. Huang Y, Wang H, Yue X, et al. Bone serves as a transfer station for secondary dissemination of breast cancer. *Bone Res*. 2023;11(1):21. doi:10.1038/s41413-023-00260-1
3. Lin Q, Wang Y, Wang L, et al. Engineered macrophage-derived cellular vesicles for NIR-II fluorescence imaging-guided precise cancer photo-immunotherapy. *Colloids Surf B*. 2024;235:113770. doi:10.1016/j.colsurfb.2024.113770
4. Desai SA, Manjappa A, Khulbe P. Drug delivery nanocarriers and recent advances ventured to improve therapeutic efficacy against osteosarcoma: an overview. *J Egypt Math Nat Cancer Ins*. 2021;33(1):4. doi:10.1186/s43046-021-00059-3
5. Tong L, Zhao Q, Datan E, et al. Triptolide: reflections on two decades of research and prospects for the future. *Nat Product Rep*. 2021;38(4):843–860. doi:10.1039/D0NP00054J
6. Wagh PR, Desai P, Prabhu S, et al. Nanotechnology-based celastrol formulations and their therapeutic applications. *Front Pharmacol*. 2021;12:673209. doi:10.3389/fphar.2021.673209
7. Martín-Ramírez R, González-Fernández R, Hernández J, et al. Celastrol and melatonin modify SIRT1, SIRT6 and SIRT7 gene expression and improve the response of human granulosa-lutein cells to oxidative stress. *Antioxidants*. 2021;10(12):1871. doi:10.3390/antiox10121871
8. Li L, Wang B, Li Y, et al. Celastrol regulates bone marrow mesenchymal stem cell fate and bone-fat balance in osteoporosis and skeletal aging by inducing PGC-1α signaling. *Aging*. 2020;12(17):16887–16898. doi:10.18632/aging.103590
9. Guo L, Zhang Y, Al-Jamal KT. Recent progress in nanotechnology-based drug carriers for celastrol delivery. *Biomater Sci*. 2021;9(19):6355–6380. doi:10.1039/D1BM00639H
10. Wang C, Dai S, Zhao X, et al. Celastrol as an emerging anticancer agent: current status, challenges and therapeutic strategies. *Biomed Pharmacother*. 2023;163:114882. doi:10.1016/j.biopha.2023.114882
11. Liu Y, Li J. Self-assembling nanoarchitectonics of size-controllable celastrol nanoparticles for efficient cancer chemotherapy with reduced systemic toxicity. *J Colloid Interface Sci*. 2023;636:216–222. doi:10.1016/j.jcis.2022.12.162
12. Luo T, Fan Z, Zeng A, et al. Biomimetic targeted co-delivery system engineered from genomic insights for precision treatment of osteosarcoma. *Adv Sci*. 2025;12(2):e2410427. doi:10.1002/advs.202410427
13. El Yakhlifi S, Ball V. Polydopamine as a stable and functional nanomaterial. *Colloids Surf B*. 2020;186:110719. doi:10.1016/j.colsurfb.2019.110719
14. Jing Y, Deng Z, Yang X, et al. Ultrathin two-dimensional polydopamine nanosheets for multiple free radical scavenging and wound healing. *Chem Commun*. 2020;56(74):10875–10878. doi:10.1039/D0CC02888F
15. Zheng P, Ding B, Li G. Polydopamine-incorporated nanoformulations for biomedical applications. *Macromol biosci*. 2020;20(12):e2000228. doi:10.1002/mabi.202000228

16. Zhan Q, Shi X, Fan D, Zhou L, Wei S. Solvent mixing generating air bubbles as a template for polydopamine nanobowl fabrication: underlying mechanism, nanomotor assembly and application in cancer treatment. *Chem Eng J*. 2021;404:126443.
17. Li Y, Li F, Pan H, et al. Targeted OUM1/PTPRZ1 silencing and synergetic CDT/enhanced chemical therapy toward uveal melanoma based on a dual-modal imaging-guided manganese metal-organic framework nanoparticles. *J Nanobiotechnol*. 2022;20(1):472. doi:10.1186/s12951-022-01643-y
18. Liu H, Xu C, Meng M, et al. Metal-organic framework-mediated multifunctional nanoparticles for combined chemo-photothermal therapy and enhanced immunotherapy against colorectal cancer. *Acta Biomater*. 2022;144:132–141. doi:10.1016/j.actbio.2022.03.023
19. Li W-Q, Wang Z, Hao S, et al. Mitochondria-targeting polydopamine nanoparticles to deliver doxorubicin for overcoming drug resistance. *ACS Appl Mater Interfaces*. 2017;9(20):16793–16802. doi:10.1021/acsami.7b01540
20. Guan BY, Yu L, Lou XWD. Formation of asymmetric bowl-like mesoporous particles via emulsion-induced interface anisotropic assembly. *J Am Chem Soc*. 2016;138(35):11306–11311. doi:10.1021/jacs.6b06558
21. Zhang L, Yang P, Guo R, et al. Multifunctional mesoporous polydopamine with hydrophobic paclitaxel for photoacoustic imaging-guided chemo-photothermal synergistic therapy. *Int J Nanomed*. 2019;14:8647–8663. doi:10.2147/IJN.S218632
22. Tu X, Joeng KS, Nakayama KI, et al. Noncanonical Wnt signaling through G protein-linked PKCdelta activation promotes bone formation. *Dev Cell*. 2007;12(1):113–127. doi:10.1016/j.devcel.2006.11.003
23. Borriello A, Caldarelli I, Speranza MC, et al. Iron overload enhances human mesenchymal stromal cell growth and hampers matrix calcification. *BBA*. 2016;1860(6):1211–1223. doi:10.1016/j.bbagen.2016.01.025
24. Ju K-Y, Lee Y, Lee S, et al. Bioinspired polymerization of dopamine to generate melanin-like nanoparticles having an excellent free-radical-scavenging property. *Biomacromolecules*. 2011;12(3):625–632. doi:10.1021/bm101281b
25. Liu H, Yang Y, Liu Y, et al. Melanin-like nanomaterials for advanced biomedical applications: a versatile platform with extraordinary promise. *Adv Sci*. 2020;7(7):1903129. doi:10.1002/advs.201903129
26. Gallo J, Villasante A. Recent advances in biomimetic nanocarrier-based photothermal therapy for cancer treatment. *Int J Mol Sci*. 2023;24(20):15484. doi:10.3390/ijms242015484
27. Zeng Y, Zhan Y, Liu X, et al. Highly efficient Chemo/Photothermal therapy alleviating tumor hypoxia against cancer and attenuate liver metastasis in vivo. *Chem Eng J*. 2022;448.
28. Hao J-N, Ge K, Chen G, et al. Strategies to engineer various nanocarrier-based hybrid catalysts for enhanced chemodynamic cancer therapy. *Chem Soc Rev*. 2023;52(22):7707–7736. doi:10.1039/D3CS00356F
29. Fukai T, Ushio-Fukai M. Cross-talk between NADPH oxidase and mitochondria: role in ROS signaling and angiogenesis. *Cells*. 2020;9(8):1849. doi:10.3390/cells9081849
30. Fang G, Tang B. Current advances in the nano-delivery of celastrol for treating inflammation-associated diseases. *J Mat Chem B*. 2020;8(48):10954–10965. doi:10.1039/D0TB01939A
31. Shi J, Li J, Xu Z, et al. Celastrol: a review of useful strategies overcoming its limitation in anticancer application. *Front Pharmacol*. 2020;11:558741. doi:10.3389/fphar.2020.558741
32. Wang L, Sun Q, Wang X, et al. Using hollow carbon nanospheres as a light-induced free radical generator to overcome chemotherapy resistance. *J Am Chem Soc*. 2015;137(5):1947–1955. doi:10.1021/ja511560b
33. Alamzadeh Z, Beik J, Mirrahimi M, et al. Gold nanoparticles promote a multimodal synergistic cancer therapy strategy by co-delivery of thermo-chemo-radio therapy. *Eur J Pharm Sci*. 2020;145:105235. doi:10.1016/j.ejps.2020.105235
34. Macchi S, Jalihal A, Hooshmand N, et al. Enhanced photothermal heating and combination therapy of NIR dye via conversion to self-assembled ionic nanomaterials. *J Mat Chem B*. 2022;10(5):806–816. doi:10.1039/D1TB02280F
35. Varaganti P, Buddolla V, Lakshmi BA, et al. Recent advances in using folate receptor 1 (FOLR1) for cancer diagnosis and treatment, with an emphasis on cancers that affect women. *Life Sci*. 2023;326:121802. doi:10.1016/j.lfs.2023.121802
36. Ai J-W, Liu B, Liu W-D. Folic acid-tagged titanium dioxide nanoparticles for enhanced anticancer effect in osteosarcoma cells. *Mater Sci Eng*. 2017;76:1181–1187.
37. Amiryaghoubi N, Abdolahinia ED, Nakhlband A, et al. Smart chitosan-folate hybrid magnetic nanoparticles for targeted delivery of doxorubicin to osteosarcoma cells. *Colloids Surf B*. 2022;220:112911. doi:10.1016/j.colsurfb.2022.112911
38. Karimian A, Yousefi B, Sadeghi F, et al. Synthesis of biocompatible nanocrystalline cellulose against folate receptors as a novel carrier for targeted delivery of doxorubicin. *Chem Biol Interact*. 2022;351:109731. doi:10.1016/j.cbi.2021.109731
39. Burke PJ. Mitochondria, bioenergetics and apoptosis in cancer. *Trends Cancer*. 2017;3(12):857–870. doi:10.1016/j.trecan.2017.10.006
40. Hong W, Park J, Yun W, et al. Inhibitory effect of celastrol on adipogenic differentiation of human adipose-derived stem cells. *Biochem Biophys Res Commun*. 2018;507(1–4):236–241. doi:10.1016/j.bbrc.2018.11.014
41. Huang S, Tang Y, Cai X, et al. Celastrol inhibits vasculogenesis by suppressing the VEGF-induced functional activity of bone marrow-derived endothelial progenitor cells. *Biochem Biophys Res Commun*. 2012;423(3):467–472. doi:10.1016/j.bbrc.2012.05.143
42. Zhang Y, Ding L, Wang T, et al. A celastrol drug delivery system based on PEG derivatives: the structural effects of nanocarriers. *Molecules*. 2023;28(3):1040. doi:10.3390/molecules28031040
43. Berger M, Toussaint F, Ben Djemaa S, et al. Poly(N-methyl-N-vinylacetamide): a strong alternative to PEG for lipid-based nanocarriers delivering siRNA (Adv. Healthcare Mater. 8/2024). *Adv Healthcare Mater*. 2024;13(8). doi:10.1002/adhm.202302712
44. Lee H, Kim MA, Lee C-M. Near-infrared laser-responsive photothermal bubble-generating PLA nanoparticles for controlled drug release. *Macromol Res*. 2021;29(3):224–229. doi:10.1007/s13233-021-9026-3
45. Zhang Q, Kuang G, Wang L, et al. Tailoring drug delivery systems by microfluidics for tumor therapy. *Mater Today*. 2024;73:151–178. doi:10.1016/j.mattod.2024.01.004
46. Li Y, Cheng Y, Wu Y, et al. Polydopamine-coated self-assembled lipid nanoparticles for highly effective chemo–photothermal combination therapy. *Ind Eng Chem Res*. 2024;63(7):3140–3151. doi:10.1021/acs.iecr.3c04310